

**Direct Prediction of the Desalination Performance
of Porous Carbons Electrodes
for Capacitive Deionization**

S. Porada, L. Borchardt, M. Oschatz, M. Bryjak, J. S. Atchison,
K. J. Keesman, S. Kaskel, P. M. Biesheuvel and V. Presser

Electronic Supplementary Information

1. Nitrogen Gas Sorption Analysis of CDC Samples

Gas sorption analysis with Nitrogen was carried out following the experimental procedure outlined in the experimental section. As seen from **Fig. S1**, the shape of the TiC-CDC isotherm is of type I (according to IUPAC classification), indicating dominant presence of micropores (i.e., < 2nm). The shape of the HIPE SiC-CDC isotherm represents the transition from type I to type V, due to sufficiently large amount of pores around 1 nm in size (**Table S1**). In this material small mesopores are present which contribute 37 vol% of the total pore volume (not including macropores). In case of OM SiC-CDC the isotherm shape is type IV including a type H4 hysteresis that proves the presence of a secondary mesoporosity along with a slit-shaped pore geometry. Very narrowly distributed micropores of 1 nm and mesopores of 4 nm are seen in **Fig. 3**; the latter encompass a pore volume of 1.5 cm³/g, and, therefore, contribute significantly to the overall pore volume of this material (**Table S1**). Macropores, which do not account to the salt electrosorption capacity, are present in all electrodes, but only in the case of HIPE SiC-CDC, such macropores are not only present between the particles but also within the particles (see also Ref. 1).

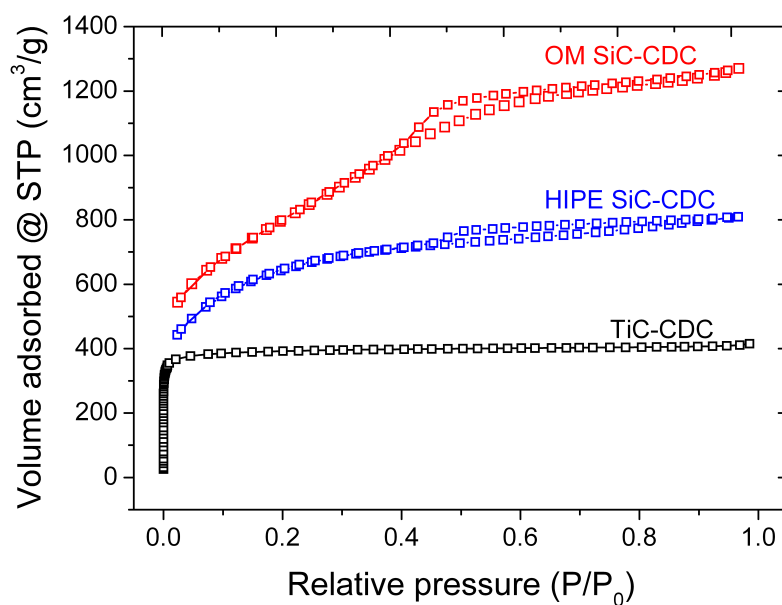


Fig. S1 Nitrogen gas sorption isotherms of TiC-CDC, HIPE SiC-CDC, and OM SiC-CDC at -196°C. STP stands for standard temperature and pressure.

Table S1 Pore volume and volume / fraction of micro- and mesopores. As defined by IUPAC, micropores are pores with a diameter smaller than 2 nm whereas mesopores are pores with a diameter between 2 and 50 nm. No macropores can be determined with the nitrogen sorption method. The pore volumes were calculated using the quenched solid density functional theory (QSDFT, Ref. 2) assuming slit-shaped pores (marked with *) or a mixed QSDFT model for slit and cylindrical pore shapes (marked with †).

	Total pore volume (mL/g)	Micropore volume (mL/g)	Fraction of micropores (%)	Mesopore volume (mL/g)	Fraction of mesopores (%)	Volume of pores smaller than 1 nm (mL/g)
TiC-CDC*	0.52	0.47	91.3	0.05	8.7	0.43
HIPE SiC-CDC [†]	1.14	0.72	63.3	0.42	36.7	0.40
OM SiC-CDC [†]	1.98	0.48	24.1	1.50	75.9	0.22

2. Raman Spectroscopy of CDC samples

Raman spectroscopy was carried out on an inVia Raman Spectrometer (Renishaw) using an excitation wavelength of 514 nm with ≤ 2 mW output power on the sample and a 50x magnification objective lens (numeric aperture: 0.75). The focus plane spot size of the laser beam was approximately 2 μm and the spectral resolution ranged from 0.8 to 1.3 cm^{-1} within the studied Raman shift range using a grating of 2400 lines/mm.

All Raman spectra showed a typical spectrum for amorphous carbon, with various degrees of ordering (**Fig. S2**, **Table S2**). Structurally, especially regarding the degree of carbon ordering, both types of SiC-CDC (i.e., OM and HIPE) are virtually identical. They also exhibit the lowest I_D/I_G band ratios which is indicative of a high degree of carbon ordering and a narrow G_2 -bandwidth of $\approx 50 \text{ cm}^{-1}$. The lower degree of carbon ordering found in TiC-CDC is exhibited by the elevated I_D/I_G band ratio but most noticeably by the broad D-band (**Fig. S2**).

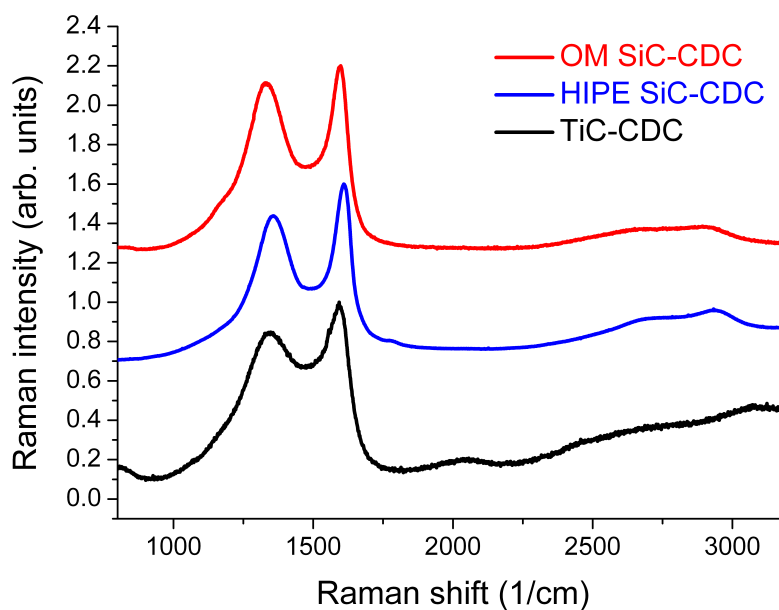


Fig. S1 Raman spectra TiC-CDC, HIPE SiC-CDC, and OM SiC-CDC

Table S2 Parameters of spectral fitting assuming a 4-peak deconvolution of the D- and G-band along with I_D/I_G band ratios (Lorentzian peak shape is assumed).

		Band position (1/cm)	FWHM (1/cm)	Peak area (arb. units)
TiC-CDC $I_D/I_G: 1.57$	D ₁	1154.7	137.1	441100
	D ₂	1343.5	185.7	4359540
	G ₁	1543.8	144.8	2092624
	G ₂	1598.8	62.2	964116
HIPE SiC-CDC $I_D/I_G: 1.22$	D ₁	1210.3	171.5	15561359
	D ₂	1358.3	125.8	73394112
	G ₁	1563.7	160.2	50542740
	G ₂	1610.0	46.2	22310958
OM SiC-CDC $I_D/I_G: 1.26$	D ₁	1179.8	135.9	3583756
	D ₂	1332.5	130.3	15820094
	G ₁	1528.7	160.1	9457017
	G ₂	1597.7	53.9	5995670

3. Salt Electrosorption Performance

Table S3 summarizes the performance of nine types of carbon materials and its BET specific surface area, total pore volume and average pore size applied for capacitive deionization. As can be seen from **Table S3**, the specific surface area as calculated by the BET method, BET SSA does not perfectly correlate with the desalination capacity of porous carbons, and the same conclusion applies to the total pore volume, volume of pores <1nm and <2nm, and the average pore size, see also **Fig. S3**.

Table S3 Selection of salt electrosorption performance reported for different electrode materials applied for CDI. AC: activated carbon; CDC: carbide-derived carbon; MWCNTs: multi-walled carbon nanotubes. All entries are sorted by ascending salt adsorption capacity per 1 g of total electrode mass. Number given per total electrode volume.

	Cell voltage (V)	Salt concentration (mg/L)	Salt adsorption (mg/g)	Salt adsorption (mg/mL ^h)	BET SSA (m ² /g)	Total pore volume (mL/g)	Average pore size (nm)	Ref.
MWCNTs	1.2	~3000	1.7	-	130	0.38	-	3
Carbon xerogel	1.2	~260	3.1	-	239	0.42	6.9	4
Microporous carbon aerogel monoliths	1.25	~2900	9.6	-	500	0.584	-	5
Norit DLC Super50 (AC)	1.2	~290	7.7	3.4	1707	0.80	1.23	this study
	1.4	~290	9.7	5.2				
Kuraray YP50-F (AC)	1.2	~290	9.1		1450	0.71	1.01	this study
	1.4	~290	11.0					
TiC-CDC	1.2	~290	10.1	5.4	1309	0.52	0.67	this study
	1.4	~290	13.3	7.2				
HIPE SiC-CDC	1.2	~290	11.1	1.2	2351	1.14	1.24	this study
	1.4	~290	13.6	1.5				
OM SiC-CDC	1.2	~290	12.8	1.6	2720	1.98	4.0	this study
	1.4	~290	16.0	2.0				

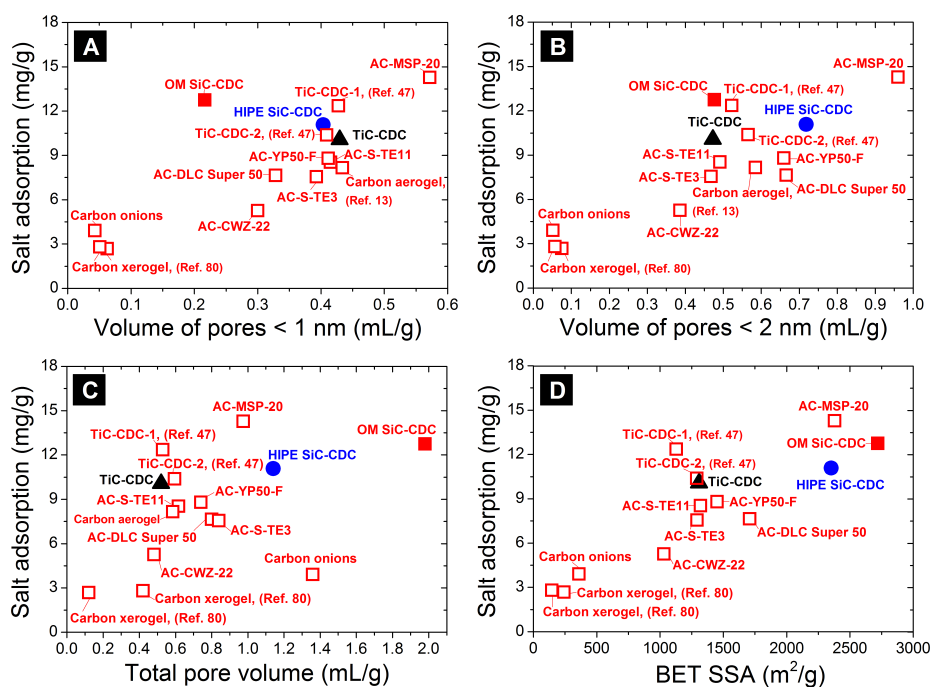


Fig. S3 Plot of electrosorption capacity versus (A) volume of pores <1nm, (B) volume of pores <2 nm, (C) total pore volume, and (D) BET SSA.

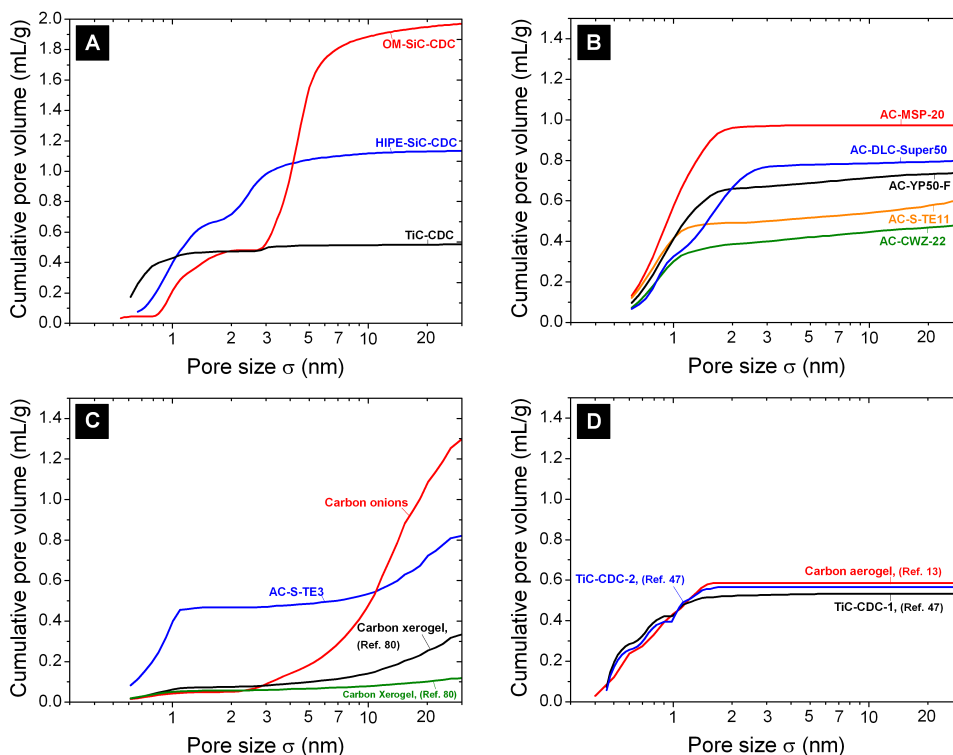


Fig. S4 Cumulative pore size distribution of the studied sample materials. Synthesized CDC materials (A), activated carbons (B), activated carbon and carbons with only outer surface (exohedral carbon; C), and comparison between TiC-CDCs and carbon aerogel (D). The data in Fig. S4A is identical with the data shown in Fig. 4 except that the data has no y-offset and, for that reason, is easier to compare.

Table S4 and S5 provide the input parameters that have been used to fit the equilibrium data with the modified Donnan model (Ref. 6).

Table S4 List of input parameter used to fit the modified Donnan model to equilibrium data of salt electrosorption Γ_{salt} and Σ_F .

	Performance ratio PR	Volumetric Stern layer capacitance at zero charge	Parameter to describe the non- linear part of the Stern capacity	Chemical attraction term for ions to go into an intra- particle pore
	(-)	$C_{\text{St,vol},0(\text{Ref})} \cdot \text{PR}$ (MF/m ³)	$\alpha_{(\text{Ref})}/\text{PR}$ (F·m ³ /mol ²)	$\mu_{\text{att},(\text{Ref})} + \ln(\text{PR})$ (kT)
TiC-CDC	2.0	144	25.0	2.7
HIPE SiC-CDC	1.0	72	50.0	2.0
OM SiC-CDC	0.666	48	33.3	1.6

Macroporosity “ p_{mA} ” (i.e., interparticle porosity) and microporosity “ p_{mi} ” (i.e., intraparticle porosity) used to describe the dynamics of salt electrosorption and charge in porous carbon electrodes were calculated according to

$$p_{mA} = \frac{d_{elec} A - (m_{elec} w_{carbon} / \rho_{carbon} + m_{elec} w_{polymer} / \rho_{polymer} + V_{mi})}{d_{elec} A} \quad (S1)$$

$$p_{mi} = \frac{d_{elec} A - (m_{elec} w_{carbon} / \rho_{carbon} + m_{elec} w_{polymer} / \rho_{polymer} + V_{mA})}{d_{elec} A} \quad (S2)$$

where d_{elec} and A stand for the thickness and exchange area of the electrode, m_{elec} , w_{carbon} , and $w_{polymer}$ are electrode mass and weight fractions of the carbons equal to 0.9 and polymer material (i.e., polymer binder added for mechanical stability) equals to 0.1. Next, ρ_{carbon} and $\rho_{polymer}$ are densities of the carbon, assumed to be constant and equal to 1.95 g/cm³ for all carbons investigated and for the carbon black used in this study, and polymer, as provided by the supplier, equals 1.78 g/cm³. Finally, V_{mi} is the volume of pores inside carbon (in transport theory called micropores), and V_{mA} is the volume of transport pathways outside the particles (called in transport theory macropores). For summary of all the geometrical measures and calculated porosities, see **Table S5**.

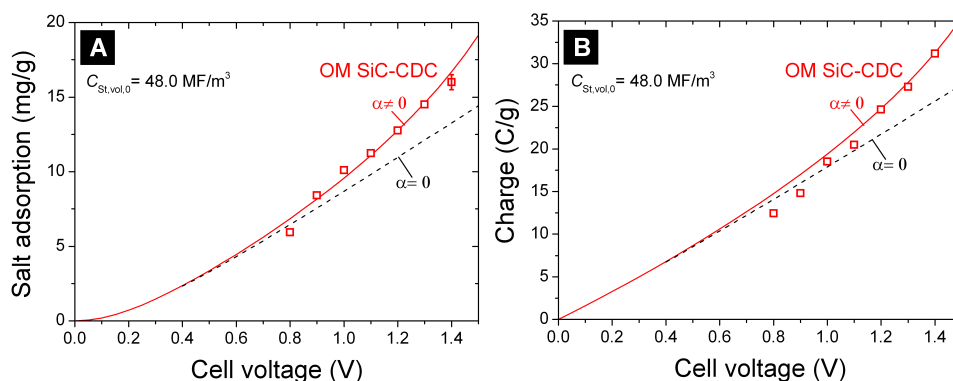


Fig. S5 Equilibrium salt adsorption and charge in porous carbon electrodes prepared from OM SiC-CDC. Lines represent fits using modified Donnan model with $\alpha=33.3 \text{ F}\cdot\text{m}^3/\text{mol}^2$ (red line) and $\alpha=0 \text{ F}\cdot\text{m}^3/\text{mol}^2$ (blue dashed line).

Table S5 Geometrical values, as used for modeling of the salt electrosorption and charge kinetics. The difference of the sum of both kinds of pores and unity represents the solid volume fraction.

	Electrode density (g/mL)	Thickness of one electrode (μm)	“Microporosity” = intraparticle pores, P_{mi} (...)	“Macroporosity” = interparticle pores, P_{mA} (...)
TiC-CDC	0.540	112	0.239	0.478
HIPE SiC-CDC	0.107	330	0.101	0.843
OM SiC-CDC	0.127	270	0.205	0.723

In the transport model, the dead volume V_{dead} is equal to 10 mL for the entire stack of 3 cells, the spacer thickness δ_{sp} is 250 μm , and the spacer porosity p_{sp} is 0.50. Finally, the ideal free solution diffusion coefficient of the average of Na and Cl is $D_{10} = 1.68 \cdot 10^{-9} \text{ m}^2/\text{s}$. However, to fit to the data we reduced this number by multiplying by a factor 0.8. Thus, in all calculations, D is taken as $1.34 \cdot 10^{-9} \text{ m}^2/\text{s}$, both in the spacer channel and in the macropores in the electrodes.

Fig. S6 (A) shows experimental data of the ion electrosorption step, after a step change in cell voltage to $V_{\text{cell}} = 0.8$ and 1.2 V. As expected, the salt concentration in the effluent water decreases rapidly reaching a minimum, after which the concentration increases again because the salt adsorption capacity of the electrode pair is slowly reached. After $t = 2000$ s, when the electrosorption step is finished, desorption takes place by setting the cell voltage to zero, which leads to rapid ion release and increase in the effluent salt concentration. **Fig. S6 (B)** shows the corresponding data of the current density from which by integration the charge transfer in C/g is calculated. **Fig. S7** shows the corresponding data at 1.4 V.

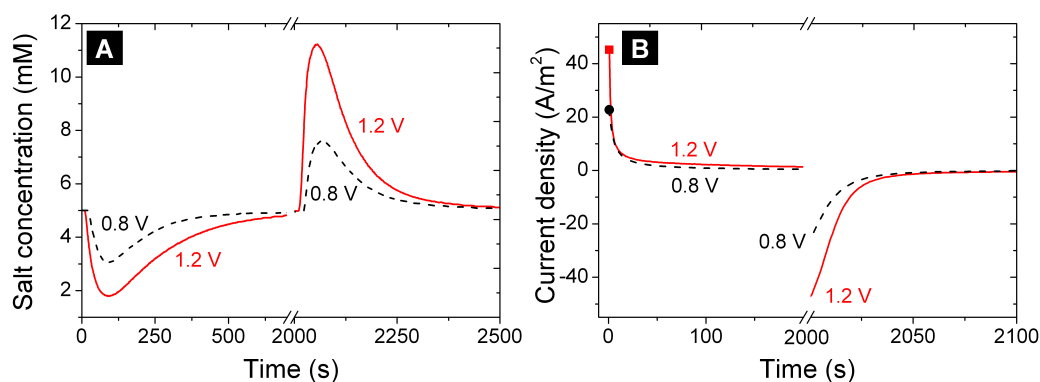


Fig. S6 Data of a single “dynamic equilibrium” CDI adsorption/desorption cycle for HIPE SiC-CDC.-(A) Effluent salt concentration and (B) Current density ($V_{\text{cell}} = 0.8$ and 1.2 V, $c_{\text{in}} = 5$ mM).

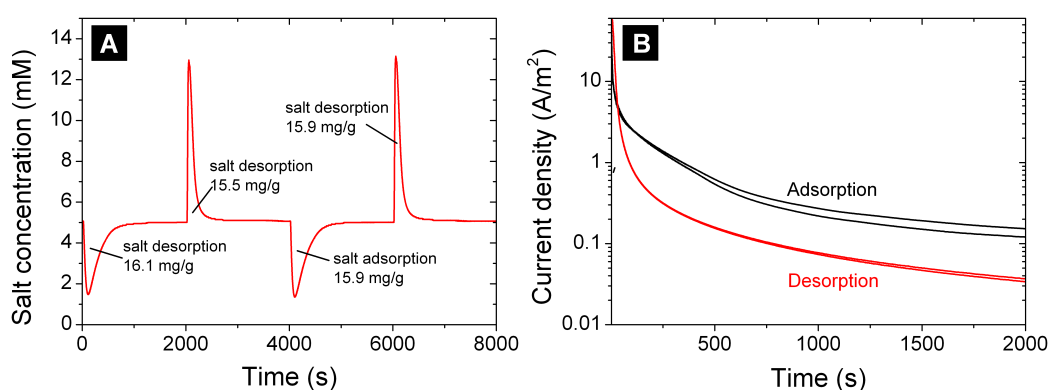


Fig. S7 Data of a single “dynamic equilibrium” CDI adsorption/desorption cycle for OM SiC-CDC. (A) Effluent salt concentration and (B) Current ($V_{\text{cell}} = 1.4$ V, $c_{\text{in}} = 5$ mM).

4. Further Theory-Data Comparison Using Two-Dimensional Porous Electrode Theory

In this section we present further data and comparison with theory for the dynamics of salt adsorption and charge formation for three CDC-materials and for two voltage levels, see Fig. S8.

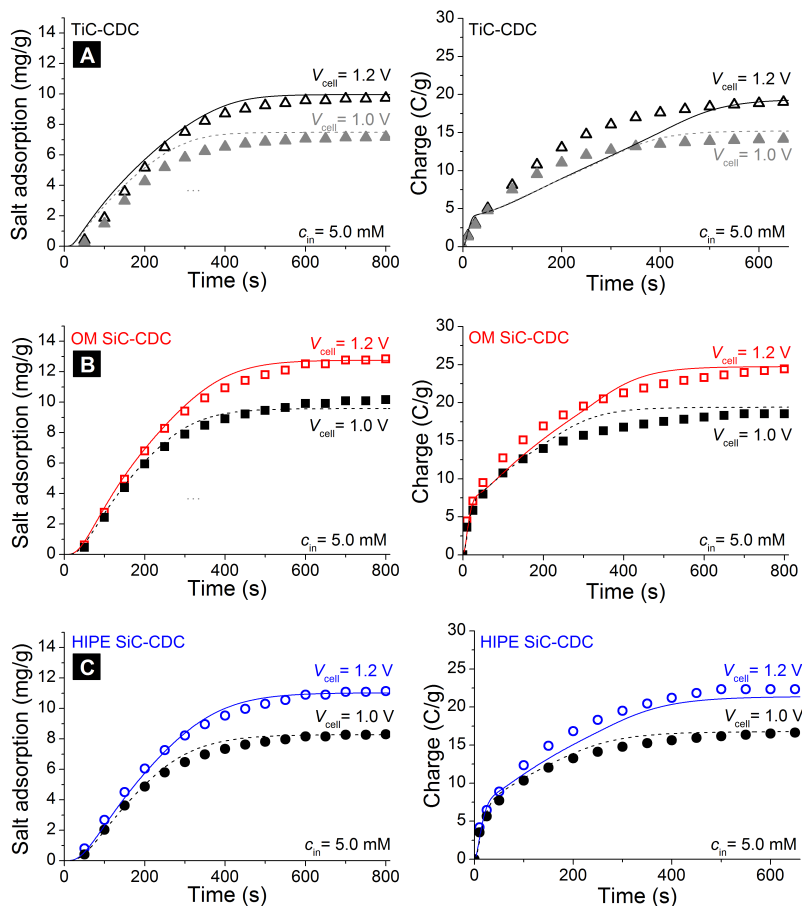


Fig. S8 Salt adsorption and charge formation in CDI cell for (A) TiC-CDC; (B) OM SiC CDC, and (C) HIPE SiC-CDC as function of time ($c_{in} = 5$ mM NaCl inflow) and cell voltage. Lines represent comparison with 2D porous electrode theory.

5. Theoretical Section

5.1 Salt Electrosorption and Charge Storage in Porous Carbon

To describe the dynamics of salt electrosorption and charge in porous carbon electrodes forming a CDI cell, we jointly consider ion transport through the space between the carbon particles, that is, the large transport pathways across the electrode (interparticle pore volume), and the electrosorption of ions inside carbon particles (intraparticle pore volume). To describe the latter, a powerful and elegant approach is to assume that the EDLs inside the intraparticle pore volume are strongly overlapping and, therefore, that the potential in these pores does not vary with position in the pore. This is the common “Donnan” approach for charged porous materials. The electrical potential in the intraparticle pore volume is different from that in the interparticle pore volume (the transport pathways) by a value $\Delta\phi_d$.

It has been recognized that the simple Donnan approach does not describe well various data sets for salt electrosorption and charge in most microporous carbons, and two modifications are required.⁶⁻⁸ The first modification is to consider the presence of a charge-free Stern layer located in between the electronic charge in the carbon matrix and the ions that reside in the water-filled intraparticle pore volume. The second modification is to include a chemical attraction energy for the ion when it transfers from the space between the carbon particles into the internal carbon pore volume, described by a term μ_{att} .⁹ Thus, in the modified Donnan model, we consider an additional, non-electrostatic, attraction for the ion to enter the pores of carbon. This attraction term also reflects the experimental reality that uncharged carbons also adsorb some salt.

The modified Donnan model containing these two modifications is described by the following equations. First of all, the volumetric concentrations (in mM= mol/m^3) of an arbitrary ion j in the pores inside a carbon particle is given by

$$c_{j,mi} = c_{mA} \cdot \exp(-z_j \cdot \Delta\phi_d + \mu_{att}) \quad (\text{S3})$$

where “mi” stands for the pores inside the carbon (intraparticle space, in transport theory called micropores), and mA for the transport pathways outside the particles (interparticle space, called macropores). Note that except for the equations in the theory-section, in the remainder of this paper we adhere to the IUPAC definition of pores,¹⁰ where the size of the pore, not the position (i.e., inside or in between carbon) defines the differentiation between micropores, mesopores, and macropores.

Considering only a monovalent salt solution, in the interparticle pores (the space within the electrode located between carbon particles), the anion and cation concentrations are equal because of local electroneutrality. Hence, $c_{j,mi}$ can be replaced by the corresponding salt concentration, c_{mA} , which will be a function of time, t (in seconds), and position x (in m) within the electrode, and $c_{j,mi}$ is a function of t and x . In Eq. S3, z_j equals +1 for the cation and -1 for the anion, while $\Delta\phi_d$ is the dimensionless Donnan electrostatic potential difference between the pores inside and in between the particles which can be multiplied by the thermal voltage, $V_T = R \cdot T / F \approx 25.7$ mV, to obtain a voltage with unit Volt.

Summing up Eq. S3 for both ions directly gives the total ion density in the pores inside a carbon particle:

$$c_{ions,mi} = c_{cation,mi} + c_{anion,mi} = 2 \cdot c_{mA} \cdot \exp(\mu_{att}) \cdot \cosh(\Delta\phi_d) \quad (S4)$$

and though it is possible to consider a different μ_{att} for anions and cations, in the present work we will assume that they are the same.

The local ionic charge density, $c_{charge,mi}$, in the pores inside a porous carbon particle follows from Eq. S3 as

$$c_{charge,mi} = c_{cation,mi} - c_{anion,mi} = -2 \cdot c_{mA} \cdot \exp(\mu_{att}) \cdot \sinh(\Delta\phi_d) \quad (S5)$$

and this volumetric charge density (in mM) relates to the Stern layer potential difference, $\Delta\phi_{St}$, according to

$$c_{charge,mi} = -C_{St,vol} \cdot \Delta\phi_{St} \cdot V_T / F \quad (S6)$$

where $C_{St,vol}$ is a volumetric Stern layer capacity in F/m^3 . Note that capital C with subscript “St,vol” is a volumetric Stern layer capacity in F/m^3 , and small c with subscript “charge,mi”, “mA”, “j,mi” is a concentration in mM. For $C_{St,vol}$ we use the expression

$$C_{St,vol} = C_{St,vol,0} + \alpha \cdot c_{charge,mi}^2 \quad (S7)$$

where the second, empirical, term reflects the experimental observation from previous work that the Stern layer capacity goes up quadratically with micropore charge, see also section 5.3.^{6,11}

The modified Donnan model equals the limit situation of the Gouy-Chapman-Stern (GCS) theory when approaching full EDL overlap in micropores where the Debye length is of the order of, or larger than, the pore size. In addition to GCS theory it includes a non-electrostatic adsorption energy μ_{att} . A difference is that in the Donnan representation EDL properties are described per unit pore volume, whereas in the GCS model charge and salt adsorption are described as function of pore area. Numbers in either definition can be converted when the pore area/volume ratio is known.

5.2 Two-Dimensional Theory for Transport and Ion Storage in Porous Electrodes

In this paper, we utilize a novel two-dimensional model for transport and storage of ions and electrical charge in a CDI cell consisting of two porous electrodes placed parallel, with a flat planar slit, or transport channel, or spacer, in between. In the direction of flow, this transport channel is mathematically divided into M subsequent sub-cells, see **Fig. 2**.¹² In the following section, we first focus on a single sub-cell, and describe ion transport in the perpendicular direction, from electrode to electrode. Next we describe how all sub-cells are combined together in a unified model for the full CDI system. We focus on a monovalent salt solution, assuming that the two ion diffusion coefficients are equal (as for KCl). Note that this is an effective diffusion coefficient for transport in the pores between the porous carbon particles that may include a contribution of pore tortuosity. Extensions to mixtures with ions of different diffusion coefficients (as must formally also be considered for NaCl) are described in Ref. 13, 14.

In the porous electrode transport model, two coupled partial differential equations must be solved along with additional algebraic equations.¹⁴⁻¹⁶ The complete model contains, as a function of the depth in the electrode x , and time t , four coupled variables: (1) the salt concentration in the pores between carbon particles, c_{mA} , (2) the electrostatic potential, ϕ_{mA} , (3) the charge density in pores inside the carbon particles, $c_{\text{charge,mi}}$, and (4) the net salt electroadsorption in such internal pores. The latter variable will be described by the effective salt concentration, c_{eff} , which is a summation of the total ion concentration times volume fraction, in the macropores and in the micropores (at location x), which we have to divide by a factor of 2 to obtain a salt concentration defined per unit total electrode volume. The effective salt concentration is thus given by

$$c_{\text{eff}} = p_{\text{mA}} c_{\text{mA}} + \frac{1}{2} p_{\text{mi}} c_{\text{ions,mi}} \quad (\text{S8})$$

where p_j is a porosity (volume fraction) defined per total electrode volume. The summation of $p_{\text{mi}} + p_{\text{mA}}$ is not equal to one, and the difference is made up of the solid matter in the electrode, such as the polymeric binder, the skeleton of porous carbon itself, and any other solid component of the carbon electrode such as conductive additives, see **Table S6**.

The porous electrode transport theory requires various geometrical measures as inputs (thickness, porosities) that can be calculated from known electrode dimensions. Besides, it requires an estimate of the diffusion coefficient of the ions in the macropores, which may be lower than the corresponding value in free solution. There are no other fitting functions related to transport part of the theory. The present model neglects a transport resistance between macropores and micropores, which can be incorporated, but will require an additional transport coefficient, see the section 5.3.

Note that the four variables for which the model is solved (i.e., c_{mA} , ϕ_{mA} , $c_{charge,mi}$ and c_{eff}) depend all on depth x and time t . It is only after sufficient time that all these variables level off to their equilibrium value, when all time derivatives become zero. This equilibrium situation can also be described directly by considering that after sufficient time (after application of a voltage signal), everywhere the macropore concentration c_{mA} has become the same as the inflow salt concentration c_0 . Then, using the modified Donnan model, we can directly calculate the equilibrium situation without having to solve the full porous electrode transport model.

The spacer channel between the two electrodes is described in the model by a series of continuously stirred tanks (sub-cells) with a salt concentration c_{sp} that is only a function of time, described by the salt mass balance

$$p_{sp} V_{sub-cell} \frac{\partial c_{sp}}{\partial t} = -J_{ions} A + \phi_v (c_{sp,in} - c_{sp}) \quad (S9)$$

where $V_{sub-cell}$ (in m^3) is the geometrical volume of the sub-cell, p_{sp} is the open porosity of the spacer channel, A the exchange area of a sub-cell with one electrode (in m^2), and ϕ_v the water volumetric flow rate running through the cell, i.e., along the electrodes (in m^3/s). We assume that the two electrodes behave symmetrically, and as a consequence the ion flux to one electrode, J_{ions} , is equal to the salt flux to both electrodes.⁸

In addition to the salt mass balance in the spacer channel, we have to specify two coupled partial differential equations that describe the transport in the porous electrode. First, within the electrode, a differential salt mass balance can be set up, given by

$$\frac{\partial c_{eff}}{\partial t} = p_{mA} D \frac{\partial^2 c_{mA}}{\partial x^2} \quad (S10)$$

with $0 < x < L_{elec}$, where L_{elec} is the electrode thickness, and D the salt diffusion coefficient in the pores between porous carbon particles. As Eq. S10 shows, we consider all fluxes to be in only one direction, namely the direction into the electrode, i.e., at cross-angles with the general flow direction of the solution through the channel, see **Fig. 2**.

The second partial differential equation describes the charge density in the intraparticle pores of carbon particles and is given by

$$\rho_{mi} \frac{\partial c_{charge,mi}}{\partial t} = 2\rho_{mA} D \frac{\partial}{\partial x} \left(c_{mA} \frac{\partial \phi_{mA}}{\partial x} \right) \quad (S11)$$

Finally, we need to solve at each position in the electrodes two algebraic equations: (1) Eq. S8; and (2) the equation for the potential ϕ_{mA} that is related to the potential ϕ_1 in the carbon matrix according to

$$\Delta\phi_d + \Delta\phi_{St} = \phi_1 - \phi_{mA} \quad (S12)$$

with expressions for $\Delta\phi_d$ and $\Delta\phi_{St}$ given by Eqs. S5, S6, and S7.

Boundary conditions required to solve the two partial differential equations are as follows. First of all, at the backside of the electrode ($x=L_{elec}$), we have $\partial c_{mA}/\partial x=0$ and $\partial \phi_{mA}/\partial x=0$. At the front-side (where $x=0$), the spacer channel concentration, c_{sp} , is equal to that in the electrode, c_{mA} . The potential gradient at $x=0$ relates to the current J , a relation which will be discussed below.

Initial conditions are as follows. At time zero, we have a certain value for c_{mA} (the same everywhere, also the same as in the spacer channel). With $c_{charge,mi}=0$ everywhere in the electrode, we can use Eq. S4 and S8 to determine c_{eff} at time zero.

To calculate voltages and currents after time zero, we must consider the overall cell voltage relationship. Namely, in the experiment we apply a voltage, V_{cell} , between the two electrodes. As explained above (see also **Fig. 2**) we assume symmetry in the CDI cell, and thus at time zero we make a step-change in applied voltage from zero to $\frac{1}{2} \cdot V_{cell}$, which is the voltage between the mid-plane in the spacer channel and that in the carbon matrix, ϕ_1 , in one of the electrodes. Note that V_{cell} has unit of Volt and must be divided by the thermal voltage, V_T , to obtain a dimensionless potential, ϕ . In the carbon matrix, we assume a constant potential ϕ_1 and thus we neglect possible electrical resistances in the carbon; in the current collectors; or in the connecting wires. This assumption is not so common in EDLC modeling, but note that in desalination the electrolyte salt concentration is typically 5 to 50 mM, much lower than the values of the order of 1 M used in EDLCs. Consequently, in CDI the ionic resistance is much more prominent than the electrical resistances for electronic charge to distribute across the electrode.

The condition of applied voltage translates directly into a relation for the potential ϕ_{mA} at the front-side of the electrode (where $x=0$), according to

$$\phi_{mA}|_{x=0} = \frac{V_{cell}}{2V_T} - \Delta\phi_{sp} \quad (S13)$$

with the voltage drop across half the spacer, $\Delta\phi_{sp}$, obtained from

$$J = -2c_{sp}p_{sp}D\frac{\Delta\phi_{sp}}{L_{sp}/2} \quad (S14)$$

where J is the current density (in mol/m²/s). Multiplying by the electrode area and by F we get a current in Ampere (note the difference between J and J_{ions}). The ions flux, J_{ions} , directed out of the spacer channel, Eq. S9, is equal to the flux into the electrode

$$J_{ions} = -2p_{mA}D\frac{\partial c_{mA}}{\partial x}\Big|_{x=0} \quad (S15)$$

and a similar boundary condition for the current density J is given by

$$J = -2p_{mA}D\left(c_{mA}\frac{\partial\phi}{\partial x}\right)\Big|_{x=0} \quad (S16)$$

In our model we consider a number of $M=6$ sub-cells placed sequentially in the direction of flow along the electrode, to describe the approximate plug-flow behavior of our system where salt and fluid are transported convectively downstream. By using a finite number of sub-cells, longitudinal dispersion is included. Note that in the model each sub-cell's electrode region is disconnected from neighboring ones. Transport from one spacer channel sub-cell to the next is described by Eq. S9, with c_{sp} the concentration in sub-cell i and $c_{sp,in}$ the concentration in the up-stream sub-cell $i-1$. The concentration in the last sub-cell ($i=M$) is equal to the effluent concentration. The sub-cell volume is equal to the total cell volume (height x electrode area) divided by the number of sub-cells, M . A small mixing volume present in the CDI unit before the conductivity sensor, is modeled using Eq. S0, with $V_{sub-cell}$ replaced by V "dead volume", with $p_{sp}=1$ and with the term $J_{ions}\cdot A$ set to zero. The current I (in A) in the stack is calculated from $I = F\cdot N/M\cdot \sum_i J_i$, where \sum_i is a summation over all sub-cells. Current I can be integrated over time to obtain the charge. Dividing by electrode mass gives us the charge per gram, Σ_F , as plotted in **Fig. 5B**, **7B**, and **8B**.

5.3 Assumptions made in the Modified-Donnan-Based Porous Electrode Theory

The porous transport theory as described in sections 5.1 and 5.2 and used in **Fig. 7** and **8** is based on various assumptions which are listed below:

- Ion transport is based on the Nernst-Planck equation for electrodiffusion which assumes ideal statistics (all activity coefficients equal to one) for ions as point charges moving in a mean electrical field. We assume the diffusion coefficient to be constant.
- Across the spacer channel we assume that concentration gradients are negligible, and thus the voltage drop across the spacer channel can be described by a simple voltage-current relation.
- We describe transport in the spacer channel in longitudinal direction (along the electrodes) by assuming a series of subsequent stirred-tanks (“sub-cells”). By taking a fairly high number of these subcells, we approximate plug-flow behavior with superimposed effects of longitudinal dispersion. This dispersion is mainly caused by the fact that the water flow velocity is not constant across the spacer thickness (direction perpendicular to flow).
- Within the electrode we assume there is only transport in the interparticle macropores, not through the intraparticle meso- and micropores. We assume that the electrodiffusional ion transport process needs only to be considered in one direction, namely the direction from spacer channel to current collector, thus across the thickness of the electrode which is the direction perpendicular to the water flow through the spacer channel. The electrode thickness is of the order of 200 μm and is much smaller than the longitudinal direction in the cell, which is of the order of 4 cm, and thus about 200-times the electrode thickness. This high ratio suggests that we can neglect the relevance of diffusional transport in the longitudinal direction.
- In addition, we neglect convective transport through the electrode in both the perpendicular and longitudinal direction. Our rationale for this assumption is that the macropores have sizes in the order of a few micrometers, much smaller than the transport paths of the order of 100 μm in size in the spacer. Thus, in the spacer the resistance to viscous flow is much less and we can expect water velocities to be much higher there than within the electrode.
- We neglect a possible transport resistance for ionic diffusion for the ion adsorption from macropores into the micropores. However, as our results presented in **Fig. 7** demonstrate, for materials without much mesoporosity, there may be such a local resistance, see Ref. 17. One option to include this effect in our model is by explicitly considering a local transport resistance between macro- and micropores. Such an approach can be based on describing the individual ion adsorption fluxes into the carbon micropores by

$$j_i = k_{\rightarrow} \cdot c_{\text{mA}} \cdot \exp(-z_i \cdot \alpha \cdot \Delta\phi_d) - k_{\leftarrow} \cdot c_{\text{mi},i} \cdot \exp(z_i \cdot (1-\alpha) \cdot \Delta\phi_d), \quad (\text{S17})$$

where α is a transfer coefficient ($0 < \alpha < 1$) and the kinetic adsorption and desorption constants, k_{\rightarrow} and k_{\leftarrow} , relate to the chemical attraction term μ_{att} according to $\mu_{\text{att}} = \ln(k_{\rightarrow}/k_{\leftarrow})$. For high values of the kinetic constants, or low values of the flux j_i , the equilibrium Donnan model is recovered.

- The modified Donnan (mD) model is used to describe the structure of the electrical double layer (EDL) in the carbon particle. Its predictions have been compared to a large range of data in Ref. 8, 13, 15, as well as in **Fig. 5** of our paper to describe both charge and salt adsorption. The mD model is the mathematical limit of the Poisson-Boltzmann equation in the limit of highly overlapped diffuse layers, valid when the ratio of Debye length to pore width is sufficiently high. In this limit, the exact pore geometry is no longer of relevance, but solely the pore volume. This is why in the mD model charge and ion adsorption are defined per unit pore volume, not per unit electrode area, which is more typical in Gouy-Chapman-Stern based EDL models. The mD model includes the fact that there is a small chemical attraction of salt into carbon micropores, via the adsorption energy term, μ_{att} , while also considering that the ionic charge and electronic charge cannot approach one another infinitely close. This effect leads to the development of a Stern layer with an associated Stern capacity in between the electronic and ionic charge. Our data in this and previous papers suggest that the capacity of this layer depends on the charge, see **Fig. S5**. To describe this effect we choose an empirical function where capacity increases according to $C_{\text{Si}} = a + b \cdot \sigma^2$ where σ is micropore charge. Such a positive dependency of Stern capacity on charge has been more often observed and reported, see Ref. 18 and 17, 19.

6. Experimental Section

6.1 CDC Materials

Titanium carbide-derived carbon (TiC-CDC) was synthesized according to Ref. 20 (**Fig. 3A**). In a quartz tube furnace (diameter: 25 mm, GERO GmbH, Germany), TiC powder (Sigma Aldrich, Germany, particle size $\approx 5 \mu\text{m}$) was heated to 600 °C in Argon (100 mL/min), then subjected to thermal treatment at 600 °C in dry chlorine gas (chlorine flow rate: 80 mL/min mixed with 70 mL/min argon) for 6 h. Then, after 1 h at 600 °C in flowing argon (150 mL/min), the sample was subjected to hydrogen treatment (80 mL/min) for 30 minutes to remove residual chlorine and metal chloride species.

Ordered mesoporous silicon carbide derived carbon (OM SiC-CDC) was synthesized according to the procedure outlined in Ref. 20 (**Fig. 3B**). A SiC polymer precursor, 6.45 g of polycarbosilane (StarPCSTM SMP-10, Starfire Systems), and 1.61 mL of para-divinylbenzene (Sigma Aldrich, 80% mixture of isomers) were drop-wise added to 6.0 g of ordered mesoporous silica (SBA-15, synthesized according to Ref. 21 and thoroughly mixed. Afterwards, the obtained mixture was evacuated over night at room temperature to obtain a homogeneous and complete pore filling. The pre-ceramic composite system was then pyrolyzed at 800 °C. Ordered mesoporous silicon carbide was obtained by removing the silica template via etching with hydrofluoric acid (33% water, 33% ethanol, and 33% of 40 mass% HF) for 3 h. The resulting OM SiC-CDC was derived after chlorine treatment of the ordered mesoporous silicon carbide materials at 800 °C. The material was heated in a quartz boat inside a quartz tube (inner tube diameter: 25 mm) in a horizontal tubular furnace (GERO GmbH) in 70 mL/min argon flow to the desired temperature (450 K/h). Subsequently, Cl₂ gas was introduced for 3 h (80 mL/min flow) while the argon flow was maintained at the same level. After that time, the Cl₂ gas flow was stopped and the sample was cooled down to room temperature in flowing argon. Residual chlorine and metal chlorides trapped in the carbon pores were subsequently removed in flowing hydrogen. For that the material was heated in a quartz boat inside quartz tube in horizontal tubular furnace in 80 mL/min H₂ flow to 600 °C for 2 h (300 K/h).

HIPE SiC-CDC was synthesized according to Ref. 1 (**Fig. 3C**). 4.37 g of SMP-10 (Starfire Systems) was mixed with 1.71 g of divinylbenzene (Sigma Aldrich, 80% mixture of isomers) under mild stirring to form the organic phase of the high internal phase emulsion (HIPE) with a volume of 6.25 mL including 30 vol% of the crosslinker. The resulting mixture was blended with 2.13 g of the nonionic surfactant SpanTM 80 (Fluka, Switzerland). After one minute, 346 mg K₂S₂O₈ (Fluka) dissolved in 18.75 mL distilled water was added drop wise to the organic phase by continuously rising up the stirring rate in order to ensure a homogeneous commingling of the phases. The resulting emulsion was then treated at 80 °C for 24 h. The removal of the surfactant was achieved by soxhlet extraction with a mixture of MeOH/water (30/70) for 24 h resulting in what we refer to as Poly-HIPE. After drying at 80 °C, the monolithic pieces of the Poly-HIPE were pyrolyzed in a horizontal alumina furnace under flowing argon at 700 °C for 2 h with a heating rate of 1 K/min. The obtained SiC monoliths were converted to carbon by thermal chlorine treatment. 2 g of the starting material were placed in a quartz boat inside a quartz tube in a horizontal tubular furnace and heated up to 700 °C with a rate of 450 K/h under an argon flow of 150 mL/min. Then, the gas flow was changed to a mixture of 80 mL/min chlorine and 70 mL/min argon. After 2 h of chlorine treatment, the furnace was cooled down to 600 °C under 150 mL/min argon and kept at that temperature for 1 h. Then, the gas flow was changed from argon to 80 mL/min hydrogen in order to remove residual chlorine and metal chlorides. This procedure was carried out for 1 h and the materials were then cooled down under argon atmosphere.

6.2 Carbon Onions

Carbon onions were prepared following the procedure outlined in Ref. 22. In short, detonation nanodiamond powder (NaBond Technologies Co. Ltd., China) with an average particle size of 4 to 6 nm was treated at 1750°C in vacuum ($\sim 10^{-7}$ bar) for 3 h. The heating and cooling rate was 10 K/min and a graphite crucible was used to hold the sample material. The resulting material was sp^2 -hybridized carbon and X-ray diffraction (XRD) analysis showed full conversion of the nanodiamond in onion-like carbon (**Fig. S9**).

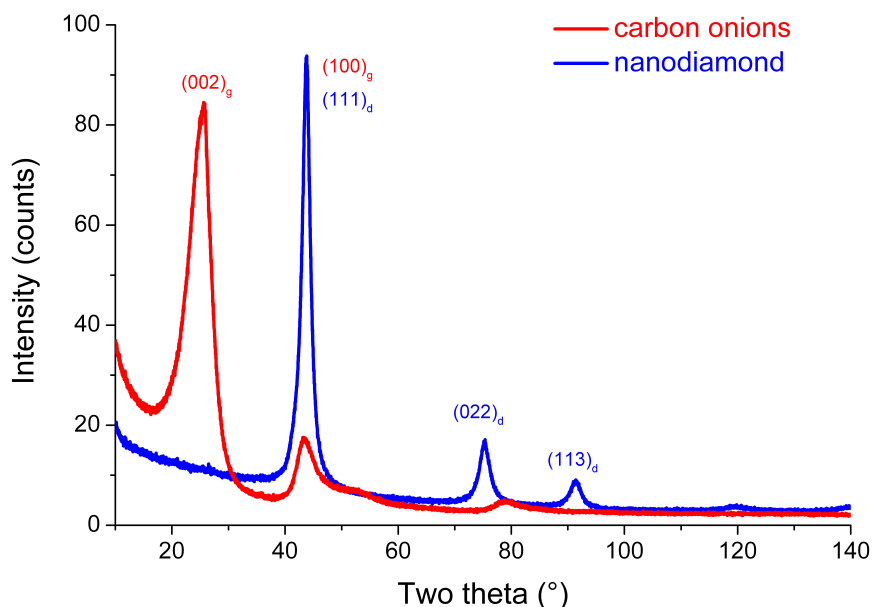


Fig. S9 XRD diffractograms of carbon onions and the precursors material, nanodiamonds. Subscript “g” denotes reflections associated with graphite and “d” denotes peaks correlating with diamond

6.3 Structural Characterization

Scanning electron microscopy (SEM) images were recorded using no sputter coating and employing a Quanta 400 ESEM (FEI, The Netherlands) in high vacuum mode at 15 kV for TiC-CDC and Gemini DSM 982 (Zeiss, Germany) at 4 kV for OM SiC-CDC and HIPE SiC-CDC.

X-ray diffraction was carried out using a D8 system (Bruker, Germany) using a Lynxeye detector. Within the 2θ range between 10 and 140 ° 2θ , the step width was 0.02 ° and the measurement time per each step was 1 s.

Prior to all gas sorption measurements, the samples were kept under vacuum (1 mbar) at 150 °C for 16 h. The porosity was analyzed using N₂ gas sorption at -196 °C up to 1 bar using an Autosorb iQ MP (Quantachrome Instruments, Germany). BET SSA values were calculated using the multipoint-BET method²³ in the linear range from 0.01-0.20 P/P₀. Total pore volumes were derived from the cumulative pore volume using the quenched solid density functional theory (QSDFT), and does not include the HIPE SiC-CDC macropores.² For HIPE SiC-CDC, and OM SiC-CDC a mixed model assuming slit and cylindrical pores was assumed, while for TiC-CDC only slit-shaped pores were considered. Slit shaped pores were also assumed for the analysis of all activated carbons. For all pore size distributions (PSDs), only the adsorption branch was used to eliminate the emergence of desorption-related artifacts.

6.4 Electrode Preparation

Electrodes were prepared following the procedure outlined in Ref. 6, except that now the electrodes were directly coated on the graphite foil current collector. First, a carbon slurry was prepared by mixing 85 mass% of CDC, 5 mass% of carbon black (Vulcan XC72R, Cabot Corp., Boston, MA), and 10 mass% of polyvinylidene fluoride (Kynar HSV 900, Arkema Inc., Philadelphia, PA); the latter had been dissolved in N-methyl-2-pyrrolidone. To obtain a homogeneous mixture, the slurry was de-aerated and stored at 50 °C for 1 h. Finally, electrodes were prepared by painting of the carbon slurry directly on one or both sides of a graphite current collector, taking care that approximately the same mass was coated on each side. The current-collector/electrode assemblies are then left for drying at room temperature. Results for thickness and total electrode mass density provided in **Table S5**. Materials AC-CWZ-22, AC-S-TE3, AC-S-TE11, and AC-MSP20 were not painted, but prepared by the wet-casting technique following procedure explained in Ref. 6.

6.5 CDI Experiments

Experimental details of the CDI test system have been described in Ref. 6, 8. In brief, a stack consisting of $N = 3$ cells is built from electrodes, current collectors, and spacers. Each current collector is coated on both sides with a layer of 6x6 cm² of the carbon electrode and is used in two adjacent cells (one above, and one below). The two current collectors at the upper and lower end of the stack only have a single layer of electrode coating. Together with open-meshed porous spacer materials (Glass fibre prefilter; Millipore, Ireland; thickness $\delta_{sp}=350 \mu\text{m}$) the current collector/electrode layers are stacked together forming three parallel cells (i.e., one stack). The flow of salt solution through the stack is kept constant at $\Phi=10 \text{ mL/min}$. The solution flows first into a housing around the stack, enters the N spacer layers from all four sides, and leaves via a centrally placed outlet (1.5x1.5 cm² channel) to flow along a conductivity meter placed in-line.

Ion electrosorption occurs when applying a voltage V_{cell} to the cell, defined as the voltage difference between the positively and negatively polarized electrodes. In our experiments, no reference electrodes are included. At the end of the salt electrosorption step, the cell voltage is reduced to zero and ion desorption begins. The electrical current running from the cathode to the anode is measured online by a potentiostat (Autolab, PGSTST30, The Netherlands) and is integrated over time to provide a measure for the total charge transferred between the electrodes. This total charge is divided by the total electrode mass in the stack, m_{tot} , to obtain the charge expressed in C/g, see **Figs. 5C, 7A, and 8A**. Parallel to the charge transfer measurements, the electrical conductivity of the effluent is measured and this value is used to calculate the effluent salt concentration and, thus, the salt removal, Γ_{salt} , see Ref. 6. The latter is calculated by integrating the difference between the inflow (c_{in}) and outflow salt concentration (c_{eff}) over time, multiplying by the flow rate Φ and dividing by m_{tot} , see **Figs. 5D, 7B, and 8B**. For each new experiment, the salt electrosorption/desorption cycle was repeated several times until the differences between cycles became negligible. We like to stress that in this work, the salt removal data is not obtained from the first cycle after a new condition has been applied, but instead is obtained when the system has reached the limit cycle, or dynamic equilibrium (DE). This important condition defines that the same amount of salt was electrosorbed during the adsorption step as was being removed in the desorption step of the cycle, as will be typical during practical long-term operation of a CDI system. All experiments were done using a $c_{\text{in}} = 5$ mM NaCl-solution (290 ppm, 550 $\mu\text{S}/\text{cm}$). The pH value of the feed solution was maintained constant at pH 7.5 during testing by automatic addition of small amounts of 0.1 M hydrochloric acid or 0.1 M sodium hydroxide to the 10 L storage vessel from which the CDI-stack was fed and to which the effluent was returned. The vessel is continuously flushed with N_2 gas to purge the water from dissolved oxygen. Note that we do not measure the conductivity decrease in this storage vessel, but in the exit tube right after the water leaves the stack, before being returned to the storage vessel. This is why after application of a cell voltage, the salinity first decreases and then goes up again, even though the voltage is still applied.

References

1. M. Oschatz, L. Borchardt, M. Thommes, K. A. Cychosz, I. Senkowska, N. Klein, R. Frind, M. Leistner, V. Presser, Y. Gogotsi and S. Kaskel, *Angewandte Chemie International Edition*, 2012, **51**, 7577-7580.
2. P. I. Ravikovitch and A. V. Neimark, *Langmuir*, 2006, **22**, 11171-11179.
3. K. Dai, L. Shi, J. Fang, D. Zhang and B. Yu, *Materials Letters*, 2005, **59**, 1989-1992.
4. J. Landon, X. Gao, B. Kulengowski, J. K. Neathery and K. Liu, *Journal of the Electrochemical Society*, 2012, **159**, A1861-A1866.
5. M. E. Suss, T. F. Baumann, W. L. Bourcier, C. M. Spadaccini, K. A. Rose, J. G. Santiago and M. Stadermann, *Energy & Environmental Science*, 2012, **5**, 9511-9519.
6. S. Porada, L. Weinstein, R. Dash, A. van der Wal, M. Bryjak, Y. Gogotsi and P. M. Biesheuvel, *ACS Applied Materials & Interfaces*, 2012, **4**, 1194-1199.
7. P. M. Biesheuvel, R. Zhao, S. Porada and A. van der Wal, *Journal of Colloid and Interface Science* 2011, **360**, 239-248.
8. S. Porada, M. Bryjak, A. van der Wal and P. M. Biesheuvel, *Electrochimica Acta*, 2012, **75**, 148-156.
9. B. Kastening and M. Heins, *Electrochimica Acta*, 2005, **50**, 2487-2498.
10. K. S. W. Sing, D. H. Everett, R. A. V. Haul, L. Moscou, R. A. Pierotti, J. Rouquerol and T. Siemieniewska, *Pure and Applied Chemistry*, 1985, **57**, 603-619.
11. S. Porada, B. B. Sales, H. V. M. Hamelers and P. M. Biesheuvel, *The Journal of Physical Chemistry Letters*, 2012, **3**, 1613-1618.
12. R. Zhao, O. Satpradit, H. H. M. Rijnaarts, P. M. Biesheuvel and A. van der Wal, *Water Research*, 2013, **47**, 1941-1952.
13. R. Zhao, M. van Soestbergen, H. H. M. Rijnaarts, A. van der Wal, M. Z. Bazant and P. M. Biesheuvel, *Journal of Colloid and Interface Science*, 2012, **384**, 38-44.
14. P. M. Biesheuvel, Y. Fu and M. Z. Bazant, *Russian Journal of Electrochemistry*, 2012, **48**, 580-592.
15. R. A. Rica, D. Brogioli, R. Ziano, D. Salerno and F. Mantegazza, *The Journal of Physical Chemistry C*, 2012, **116**, 16934-16938.
16. R. A. Rica, R. Ziano, D. Salerno, F. Mantegazza, M. Z. Bazant and D. Brogioli, *Electrochimica Acta*, 2013, **92**, 304-314.
17. R. K. Kalluri, M. M. Biener, M. E. Suss, M. D. Merrill, M. Stadermann, J. G. Santiago, T. F. Baumann, J. Biener and A. Striolo, *Physical Chemistry Chemical Physics*, 2013, **15**, 2309-2320.
18. D. C. Grahame, *Chemical Reviews*, 1947, **41**, 441-501.
19. M. Z. Bazant, K. T. Chu and B. J. Bayly, *SIAM Journal on Applied Mathematics*, 2005, **65**, 1463-1484.
20. E. Kockrick, C. Schrage, L. Borchardt, N. Klein, M. Rose, I. Senkowska and S. Kaskel, *Carbon*, 2010, **48**, 1707-1717.
21. M. Choi, W. Heo, F. Kleitz and R. Ryoo, *Chemical Communications*, 2003, 1340-1341.
22. J. K. McDonough, A. I. Frolov, V. Presser, J. Niu, C. H. Miller, T. Ubieto, M. V. Fedorov and Y. Gogotsi, *Carbon*, 2012, **50**, 3298-3309.
23. British Standards, BS ISO 9277 Determination of the specific surface area of solids by gas adsorption - BET method, 2010.